

# Fault slip and rupture velocity inversion by isochrone backprojection

Gaetano Festa<sup>1,2</sup> and Aldo Zollo<sup>1</sup>

<sup>1</sup>RISSC-Lab, Department of Physics, University Federico II, Naples, Italy

<sup>2</sup>Institut de Physique du Globe de Paris, Paris, France. E-mail: festa@ipgp.jussieu.fr

Accepted 2006 April 20. Received 2006 April 20; in original form 2005 May 10

## SUMMARY

A new technique is proposed here for the retrieval of slip images from the backprojection of high-frequency displacement records. When direct  $S$  waves are seen to be dominant in the near-source data, Green functions can be approximated by the far-field terms, as described by ray theory. Assuming that the slip rapidly reaches the final value (i.e. short slip duration), the measured displacement can be ascribed to the slip contributions lying on the corresponding isochrone on the fault plane. Here we use the far-field representation theorem to backproject on the fault plane the displacement amplitudes measured along the seismogram. Through the weighted stack of amplitude maps obtained from different stations we recover high slip zones on the fault.

The resolution analysis of the backprojected images is realized with spike tests (that we refer to as ‘image Green functions’), which revealed to be an useful tool for detecting and locating artificial distortions of high slip patches, due to a poor data coverage. However, when the slip is uniformly spread along the isochrones, energy is scattered everywhere on the fault, leading to defocusing effects on the final images. A partial deconvolution technique is proposed by reiterating the backprojection. An important implication of this study is that slip maps can be obtained as functions of the rupture time on the fault, that is, the method can be used to retrieve variable rupture velocity kinematic models. Since the latter parameter is not known *a priori*, we suggest that a data set of coupled rupture velocity and slip maps is built up and the optimal model is chosen according to a waveform fitness criterion. This procedure allows the slip inversion to be separated from the rupture velocity inversion, significantly reducing the number of parameters to be estimated. Additionally, the parametrization of the rupture velocity is done on a less dense grid than the slip.

By way of example, the technique is applied to estimation of the kinematic rupture model of the 2000 Tottori earthquake ( $M = 6.8$ ), based on the inversion of near-source strong-motion data.

**Key words:** fault model, fault slip, inverse problem, ray theory, rupture propagation, slip inversion, tomography.

## 1 INTRODUCTION

Source properties are required to throw light on the mechanisms of earthquake rupturing as well as on the estimation of the strong ground motion. Full dynamic inversions (Peyrat & Olsen 2004) today need a large amount of recorded data in the vicinity of the source, more robust theoretical support and hard computation, which are not always available. A purely kinematic approach is indeed preferred, because it has the major advantage of limiting the number of retrievable parameters to the final slip distribution, the rupture velocity and the slip duration (the rise time). In this description, the macroscopic properties are presumed to be known (the total seismic moment and the fault mechanism, the geometry and the dimensions) or they are assumed [the shape of the source time function (STF)].

To estimate the amplitude of slip occurring along the fault from the observed records, seismologists generally use the representation theorem. This allows for the computation of the ground motion displacement  $\mathbf{u}(\mathbf{x}, t)$  in any point of the medium, as a function of the dislocation  $\delta\mathbf{u}$  on the fault  $\Sigma$ , without introducing specific fracture models (see e.g. Aki & Richards 1980):

$$u_n(\mathbf{x}, t) = \int_{-\infty}^{\infty} d\tau \int_{\Sigma} \delta u_i(\boldsymbol{\xi}, t) c_{ijpq} n_j \frac{\partial G_{np}(\mathbf{x}, t - \tau; \boldsymbol{\xi}, 0)}{\partial \xi_q} d\boldsymbol{\xi}, \quad (1)$$

Here,  $\mathbf{c}$  is the elastic coefficients tensor,  $\mathbf{n}$  is the normal to  $\Sigma$  and finally  $\mathbf{G}$  is the Green function tensor, that is, the response of the medium to an unidirectional unit impulse.

The separation of contributions coming from the source and the structure is not an easy matter, when looking at the seismic records.

However, seismological observations of the rupture process associated with crustal earthquakes, suggest a dominant effect of the rupture process on the seismic radiation in the near source range, that is, at distances comparable to the fault length and at low frequencies ( $f \leq 1$  Hz) (Heaton 1990; Anderson 1991; Koyama 1997).

Most of inversion techniques use either the discrete wavenumber method (Bouchon 1979) or the ray theory (see e.g. Chapman 1985) to numerically compute the Green functions. The latter method is a high-frequency asymptotic expansion representing the dominant contribution of the complete wavefield, in the far-field condition at near-source distances (Farra *et al.* 1986; Beroza & Spudich 1988). When dense seismic networks allow for the retrieval of the precise locations and focal mechanisms of the aftershocks, the Green functions can be obtained empirically (EGF) from microearthquake records, when they have the same geometric properties as the main event (Hartzell 1978). However, in the inversion of high-frequency signals, inaccurate description of the velocity structures may significantly affect the estimates of the source parameters (Graves & Wald 2001).

The knowledge of the Green functions allows to uncouple the propagation from the source. From the pioneering work of Aki (1968) significant contributions have improved the inversion techniques aimed at estimating the slip history on the fault during the rupture process. Classical methods adopt a linearized approach in the time domain (Beroza & Spudich 1988) or in the frequency domain (Cotton & Campillo 1995) and they may combine different data sets, such as strong motion and teleseismic records, geodetic measurements and surface observations (Wald & Heaton 1994).

However, linearized techniques provide solutions which are strongly dependent on the initial choice in the parameters space. This has led to the development of fully non-linear approaches, in which the distance between the data and the synthetics is minimized according to a cost function, through a global search in the parameters space. Most popular techniques are the simulated annealing (Hartzell & Liu 1995; Ji *et al.* 2001), the neighbourhood algorithm (Kennett *et al.* 2000) or the genetic algorithm (Zeng & Anderson 1996; Zeng & Chen 2001; Emolo & Zollo 2005). The choice of an optimal algorithm is still a debated question, but a global search generally penalizes the convergence to the solution. Nearby the minimum the search can be accelerated by using a local exploration technique, such as the downhill simplex (Hartzell & Liu 1995; Vallée *et al.* 2003).

In this paper, we present a new technique that addresses the issue of retrieving seismic slip images from isochrone backprojection of high-frequency records. The concept of isochrone was introduced by Bernard & Madariaga (1984) and Spudich & Frazier (1984) who proposed an approximated formula for the representation integral (1), that is valid at high frequencies and for short rupture rise times. Starting from the inverse problem as stated by Beroza & Spudich (1988), we decouple the inversion of the slip, which is retrieved by simple backprojection, from the one of the rupture velocity, which still constitutes the kernel of the inversion algorithm. In the first section, the grounds for the methods are detailed for both continuous and discrete representations. The quality of the slip images is analysed in terms of the approximations and resolution (Sections 3 and 4). Subsequently the inversion kernel is discussed in Section 5. All the steps of the methodology, within the approximations have been described through synthetic examples based on the source-station distribution of the 2000 October 6 Tottori ( $M = 6.8$ ), Japan, earthquake. Finally, an application to real data of the same earthquake is presented in Section 6.

## 2 THE 2000 TOTTORI EARTHQUAKE

The 2000 October 6, Western Tottori earthquake ( $M_w = 6.8$ ) originated at 04:30:18.07 UTC, 35.27N, 133.35E, and propagated through the digital networks K-net and Kik-net, with several records in the vicinity of the fault (almost 20 stations are located at less than 50 km from the epicentre). The depth of the earthquake has been estimated to range between 11 and 15 km (Japan Meteorological Agency, Iwata & Sekiguchi 2002; Fukuyama *et al.* 2003; Semmane *et al.* 2005). According to the aftershock relocation, the rupture propagated bilaterally, along an almost vertical plane at about 145N with a bending to 165N in the last 5, 10 km northwards (Fukuyama *et al.* 2003). The moment tensor (CMT) indicates a pure strike-slip solution.

For this study, we choose a simplified fault geometry with a rectangular area of length 30 km, width 20 km, the hypocentre located at 13.5 km of depth and angular parameters *strike* = 150N, *dip* = 90 and *rake* = 0. Since there was no evidence of surface slip observed in the main shock area, we set the depth of the top of the fault at 1 km, as suggested by Peyrat & Olsen (2004). We also adopt a simplified 1-D propagation model, such as that defined in Iwata & Sekiguchi (2002). The specific parameters for all of the layers are detailed in Table 1. Some other 1-D models that differ from this one mainly in the shallower layering, do not have a significant influence in the computation of the Green functions. Fukuyama *et al.* (2003) have already observed no relevant variations for the aftershock relocation, when testing different 1-D propagation models. This allows for a robust computation of the traveltime between the stations and the subfaults. Finally, the location of the stations, as used in the application, is listed in the Table 2, while the source-station geometry is sketched in Fig. 1.

## 3 ISOCHRONE BACK PROJECTION

In the high-frequency far-field approximation, the representation theorem (1) can be reduced to a line integral, if the slip is assumed

**Table 1.** 1-D propagation model used in the simulations. For a given layer,  $d$  is the depth of the top interface,  $c_p$  and  $c_s$  are  $P$  and  $S$ -wave velocities, respectively, and  $\rho$  is the density.

$d$ (km)	$c_p$ (km s <sup>-1</sup> )	$c_s$ (km s <sup>-1</sup> )	$\rho$ (g cm <sup>-3</sup> )
0	5.5	3.18	2.6
1.9	6.0	3.5	2.7
16	6.6	3.81	2.8
38	8.0	4.62	2.9

**Table 2.** Station names and coordinates in latitude/longitude reference frame.

Name	Longitude (E)	Latitude (N)
OKYH08	133.5581	34.8671
OKY004	133.6044	34.9547
SMNH10	133.448	35.5547
SMNH12	132.9583	35.160
SMN001	133.2638	35.5341
SMN002	133.1708	35.4683
SMN003	133.2355	35.1463
SMN004	133.003	35.285
TTR006	133.73	35.5075
TTRH04	133.733	35.4636
SMNH02	133.1782	35.2203
HRS021	133.2197	34.9497

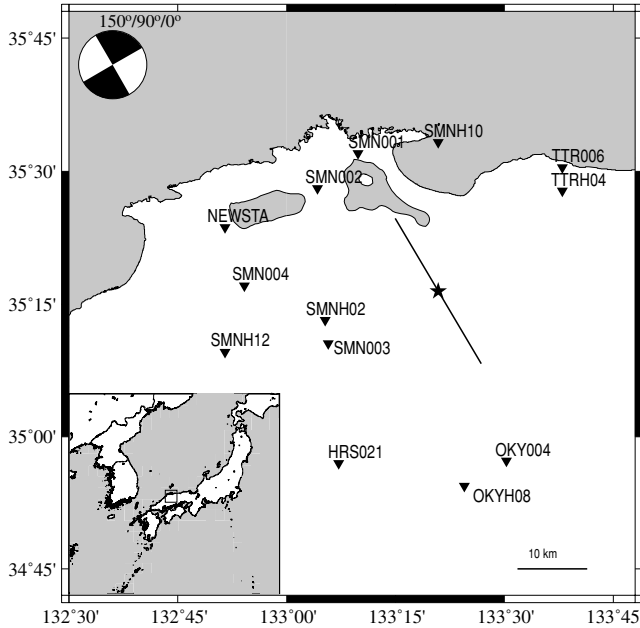


**Figure 1.** Fault geometry for the 2002, Tottori earthquake, and station set, as used for the backprojection. The star indicates the epicentre. The station NEWSTA is fictitious and has been used only in the synthetic tests to illustrate the method.

to reach its final value instantaneously (the STF is a delta function) (Bernard & Madariaga 1984; Spudich & Frazier 1984).

For a horizontally layered medium, consider the quantity

$$\mathcal{U}_i^c(\mathbf{x}, t) = \int_{\mathcal{L}} K^c \frac{R_{ij}^c(\mathbf{x}, \boldsymbol{\xi})}{r^c(\mathbf{x}, \boldsymbol{\xi})} \delta u_j(\boldsymbol{\xi}) \mathcal{C}(v, c, \phi) d\boldsymbol{\xi}, \quad (2)$$

where the superscript  $c$  individuates one seismic phase ( $P$  or  $S$ ),  $\mathbf{R}^c$  is the radiation pattern, which depends on the orientation of the fault,  $r^c$  is the geometric spreading and  $K^c$  is a constant value, defined as

$$K^c = \frac{1}{4\pi \sqrt{\rho \rho_0 c c_0^5}} F_c^c. \quad (3)$$

In the expression above,  $\rho_0$  and  $\rho$ ,  $c_0$  and  $c$  are the density and wave velocity values at the source and at the receiver, respectively, and  $F_c^c$  is a complex value, that accounts for the free surface and transmission/reflection coefficients.

Finally, the Doppler contribution  $\mathcal{C}$ , due to the directivity, is:

$$\mathcal{C} = \frac{v c}{c - v \cos(\phi)}, \quad (4)$$

where  $v$  is the rupture velocity and  $\phi$  is the angle between the direction of the point  $\boldsymbol{\xi}$ , as seen from the hypocentre, and the direction of the observer  $\mathbf{x}$ , as seen from  $\boldsymbol{\xi}$ .

The final displacement can be retrieved by accounting for the phase shifts:

$$u_i^c(\mathbf{x}, t) = \text{Re}(\mathcal{U}_i^c(\mathbf{x}, t)) - \text{Im}(\mathcal{H}[\mathcal{U}_i^c(\mathbf{x}, t)]), \quad (5)$$

where  $\mathcal{H}$  is the Hilbert transform operator.

The integral path is a curve  $\mathcal{L}(t)$  on the fault, referred to as the ‘isochrone’. Each point of this curve satisfies the elliptical relationship:

$$T_p(\mathbf{x}, \boldsymbol{\xi}) + T_r(\boldsymbol{\xi}) = \text{const}, \quad (6)$$

where  $T_p$  is the traveltimes (propagation time along the  $P$  or  $S$  travel-paths from the point source  $\boldsymbol{\xi}$  to the receiver at  $\mathbf{x}$ ) and  $T_r$  is the

rupture time (the time needed by the rupture front to reach  $\boldsymbol{\xi}$  from the hypocentre). Moreover, the isochrones are closed concentric curves, if supershear and rupture velocity inversions are forbidden on the fault.

If the displacement  $\mathbf{u}$  has been measured at a set of receivers on the free surface, we can invert eq. (5) to retrieve the slip function on the fault. As a first-order approximation, the slip direction (rake) can be assumed to be constant and, as a consequence, the slip distribution reduced to a scalar function. In this case, the three components of a seismogram will furnish independent information about the slip from the same point of view.

Finally, the Hilbert transform contribution (the imaginary part in eq. 5) is assumed to be negligible. This is a reasonable hypothesis, since the Hilbert contribution is a zero mean, non-causal contribution and it is expected to poorly affect the recorded displacement. This contribution will be discussed in more detail later.

With the above approximation, the isochrone theorem can be stated as follows:

$$u_i^c(\mathbf{x}, t) \approx \int_{\mathcal{L}} \text{Re}(K^c) \frac{R_{ij}^c(\mathbf{x}, \boldsymbol{\xi})}{r^c(\mathbf{x}, \boldsymbol{\xi})} \gamma_j \delta u(\boldsymbol{\xi}) \mathcal{C}(v, c, \phi) d\boldsymbol{\xi}, \quad (7)$$

where  $\mathbf{u}$  is the effective recorded displacement and  $\gamma_j$  is the  $j$ th component of the unit vector that has the direction of the slip. If the rupture velocity is known on the fault surface, the map of the isochrones can be formed. From eq. (6), the rupture times can be evaluated by using a finite difference approximation of the eikonal equation (Podvin & Lecomte 1991) and the propagation times by shooting rays from the subfaults to the receivers.

According to eq. (7), the observed amplitude on the displacement record at a given time  $t$  represents the sum of the contributions lying on the corresponding isochrone  $\mathcal{L}(t)$ , propagated to the receiver. If we had only one receiver, for a given recorded amplitude at time  $t$ , we would be not able to distinguish which points of the corresponding isochrone provided effective dislocation. Increase of resolution is achieved when intersecting information coming from several receivers, the associated maps of isochrones of which scan the fault plane along different paths. Consider the stations SMN001 and NEWSTA in the Fig. 1 (NEWSTA is a fictitious station, used only in this example). Also assume a homogeneous slip on the fault as well as a homogeneous propagation model, with  $c_s = 3.5 \text{ km s}^{-1}$ . At the directive station SMN001 (Fig. 2, column a), the largest amplitudes are recorded, with the displacement expected without any change of sign, since the receiver is always seen on the same side by the advancing rupture front. On the fault, the isochrones are lengthened in the hypocentre-to-receiver direction. At the lateral station NEWSTA (Fig. 2, column b) the amplitudes are one order of magnitude lower and the changes of sign in the trace occur because the station, as seen from different points on the fault, crosses the  $S$  nodes of the focal mechanism (at  $45^\circ$  from the  $P$  nodes, plotted in Fig. 1). In correspondence, the isochrones on the fault have an almost circular shape. Trajectories on the fault plane significantly depend on the position of the hypocentre (Fig. 3a) but not on the propagation model. In Fig. 3(b) isochrones have been sketched for the station SMN001 and the 1-D model of Table 1.

The basic concept of the backprojection is thus to interpret the displacement records as slip on the fault, after a suitable correction for the propagation effects.

Denote with  $A_j(t_i)$  the observed amplitude at time  $t_i$  on the displacement record at the  $j$ th receiver. In correspondence, the isochrone  $\mathcal{L}_{ij}$  can be drawn on the fault plane. Since no *a priori* knowledge of the slip function is available, the slip is assumed to be uniform along the isochrone ( $\delta u^{\text{iso}}$ ); in this case, the observed

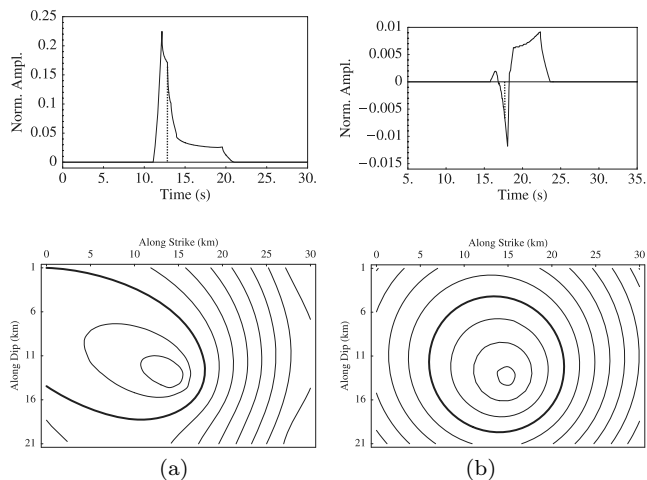


**Figure 2.** Displacement records for the station SMN001 (East component) and NEWSTA (North comp.) and corresponding isochrones maps on the fault plane. Units on the traces need to be scaled as a function of the slip, which is assumed unitary. For the directive station (panel a), the isochrones are lengthened along the source–receiver direction and their amplitude is significantly larger because of the directivity. For the lateral station (panel b), the amplitudes are lower and the shape of the isochrones is pretty circular. Isochrones have been enhanced on the fault in correspondence of the times marked on the signals.

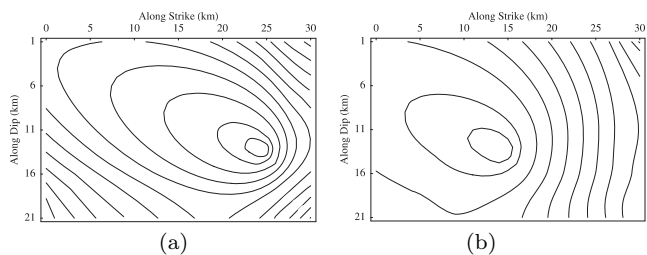


**Figure 3.** Isochrones map for the station SMN001, when the hypocentre is displaced to the south (panel a) and for the 1-D velocity model (panel b), as described in Table 1.

amplitude would be:

$$A_j(t_i) = \delta u^{\text{iso}} \int_{\mathcal{L}_{ij}} \text{Re}(K^c) \frac{R_{jh}^c(\mathbf{x}_j, \boldsymbol{\xi})}{r^c(\mathbf{x}_j, \boldsymbol{\xi})} \gamma_h C(v, c, \phi) d\boldsymbol{\xi}. \quad (8)$$

The quantity

$$L_{ij} = \int_{\mathcal{L}_{ij}} \text{Re}(K^c) \frac{R_{jh}^c(\mathbf{x}_j, \boldsymbol{\xi})}{r^c(\mathbf{x}_j, \boldsymbol{\xi})} \gamma_h C(v, c, \phi) d\boldsymbol{\xi}, \quad (9)$$

depends only on the geometric properties of the fault and the propagation medium, which are assumed. This is the scaling factor of the observed amplitude, that is used to retrieve the slip function  $P_j(\boldsymbol{\xi})$ , as seen from the  $j$ th receiver:

$$P_j(\boldsymbol{\xi}) = \frac{A_j(t_i)}{L_{ij}} \quad \boldsymbol{\xi} \in \mathcal{L}_{ij}. \quad (10)$$

There is no ambiguity in the definition of  $P_j$ , since each point of the fault is crossed by a unique isochrone in the assumption of a zero rise time.

Again, we note that the contribution coming from different components of the same station to the slip function should be the same, with the differences in the records being taken into account only through the radiation pattern.

Adding the contributions from all of the stations, the slip map, as retrieved by the backprojection, is:

$$B(\boldsymbol{\xi}) = \sum_{j=1}^N w_j P_j(\boldsymbol{\xi}), \quad (11)$$

where  $N$  is the number of stations and  $w_j$  are suitable weights. They are indicative of the quality of the signal with respect to the noise and they can be associated to some punctual measurement, as the maximum amplitude, or to some global indicator, as the energy content.

The fault discretization is introduced by subdividing its surface into elementary subfaults, in which the slip is assumed to be uniform. The cell size should be small enough to warrant a Fraunhofer approximation, that is, the subfaults should be viewed as point sources by the receivers.

In the discrete case, for a given receiver, each subfault is expected to be crossed by more than one isochrone because its size should be larger than the sample spacing of the isochrones on the fault. The slip function there, is the average of the contributions carried by the points inside that subfault. The total ‘brightness’ can be achieved by using the same formula (11), providing that the receiver brightness is that of the subfaults and not of the single points.

During the backprojection, we should pay attention to the value of the contribution  $L_{ij}$ , which is the denominator in the eq. (10). For small  $L_{ij}$ , instabilities can occur when the level of the noise is relevant with respect to the signal. From a Singular Value Decomposition (SVD) point of view, it corresponds to the amplification of the solutions with small eigenvalues. The contribution  $L_{ij}$  may be relatively small in the vicinity of the hypocentre (where the total length of the isochrone is small) or when the station crosses the nodes of the radiation pattern, as seen from different points along the same isochrone. In the latter case, their contributions will interfere destructively, reducing the apparent length of the isochrone  $L_{ij}$  itself (eq. 9). To warrant stability to the projection, we regularize the solution nearby the hypocentre by a smoothness operator and we skip the backprojection of the amplitudes, when the radiation-pattern changes sign along the corresponding isochrone. Moreover, positivity constraint is simply imposed by assuming zero slip, when the latter tries to be negative.

The slip maps from the backprojection are derived assuming a zero rise time (eq. 11). However, for a finite rise time  $\tau(\boldsymbol{\xi})$ , an equivalent formulation can be proposed: in this case, the representation theorem (1) is reduced to a surface integral bound by two isochrones that correspond to times  $t$  and  $t - \tau$ , if  $\tau$  is constant on the fault (Zollo & Bernard 1989). If it is allowed to vary, the isochrones will be stretched and they can no longer be closed curves where additional smoothness constraints are not imposed. However, assuming a smooth variation of the rise time on the fault plane, its effect is a low-pass filter on the slip image with cut-off wavelength of  $v\tau$ , and a delay of  $\tau$  in the maximum value of the slip.

This backprojection technique is analogous to medical tomography imaging (TAC), which is interpreted analytically as a *radon transform*. The radon function computes projections of a bidimensional function  $f(x, y)$  along specified directions. This projection is a set of line integrals that are evaluated along parallel paths. The complete radon transform is indeed the collection of these 1-D functions, computed for all the directions.

In our method, the slip function  $\delta u$  has the role of the original function  $f$ , and line integrals are represented by the isochrone integrals (7). The direction is identified by the position of the receivers

with respect to some reference point on the fault (conventionally the hypocentre). Some trials of inverting the radon-transform directly to retrieve the slip function have been applied to small earthquakes (Bindi & Caponetto 2001) when the STF can be satisfactorily retrieved using empirical Green functions.

### 3.1 Hilbert contribution

When using the expression (7) instead of (5), the Hilbert transform contribution is automatically neglected. The latter cannot be backprojected on the fault. Because of its convolutional feature, it combines information from everywhere on the fault to achieve the displacement amplitude at a given time.

For an assigned function  $f(t)$ , the Hilbert transform is:

$$\mathcal{H}[f(t)] = -\frac{1}{\pi} \int_{-\infty}^{\infty} \frac{f(\tau)}{t - \tau} d\tau, \quad (12)$$

with the associated transfer function  $-\frac{1}{\pi t}$ , which is different from zero everywhere on the  $t$  axis. As a consequence, a function assuming a zero value for  $t \leq t_0$  would have the Hilbert transform different from zero also for  $t \leq t_0$ , losing the causality. Thus, this term is expected to be a small contribution, that has little effect on the displacement amplitudes.

On the other hand, this contribution is due to the critical and supercritical incidences of the seismic rays, that are emphasized at the farthest stations, outside the shear-wave window, when the motion becomes elliptical. The relevance of the Hilbert contribution should be numerically tested for the fault-station geometry, assuming, for example, uniform slip and rupture velocity on the fault. The same check can be provided on the data, looking at the particle motion.

## 4 IMAGE PROCESSING

### 4.1 Defocusing

In medical imaging, high resolution is guaranteed by the azimuthally uniform scanning of the target. For seismic slip images, instead, the lack of resolution can be ascribed to the limited number of stations and their mutual positions with respect to the hypocentre, along with the inaccurate correction for path effects and the focal mechanism. Since we assume that the slip is uniformly distributed along the isochrones, for any receiver, high slip zones are effectively expected to be retrieved by intersecting the contributions of the different stations. However, energy is still spread out elsewhere on the fault. We illustrate the steps of the backprojection for the Tottori fault-station distribution of Fig. 1. In this synthetic example, the slip is assumed to be uniformly zero on the fault, apart from a square anomaly located on the north-west side of the fault, in which the value is  $\delta u = 5$  m. The boundaries of the anomaly have been superimposed on the snapshots of Fig. 4. Rupture velocity is also uniform ( $v = 2.8 \text{ km s}^{-1}$ ) and the propagation model is the one of Table 1. The fault has been discretized in  $30 \times 20$  square elements and for any receiver, the isochrones have been approximated inside any subfault with piecewise linear curves (Discretization for the isochrones times is 10 times finer than the size of the subfault). For sake of simplicity, we select only six stations (SMNH12, SMN004, SMN001, TTR006, OKY004, HRS021), which scan the fault plane from independent points of view. The Green functions have been computed using the same approximation as in the backprojection (direct  $S$  wavefield from ray theory), to single out the effects of the backprojection.

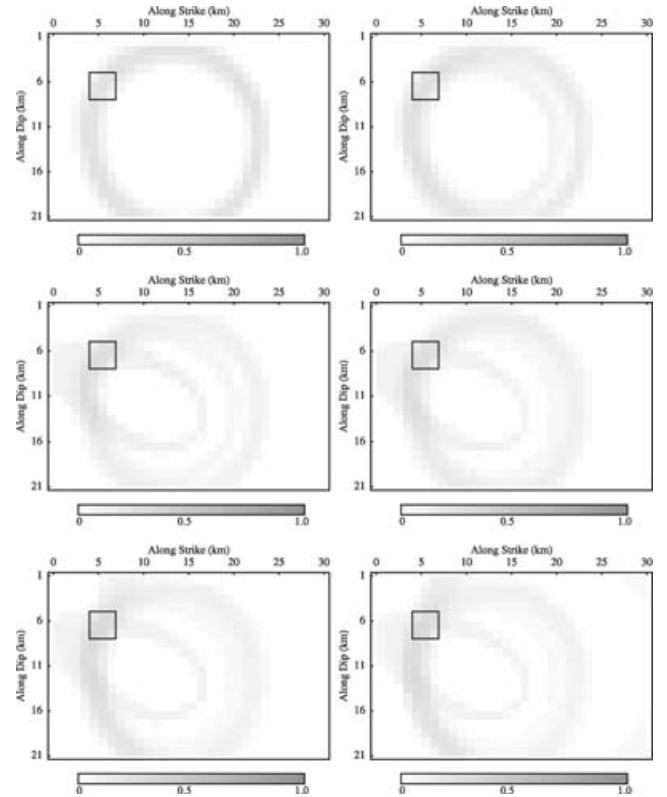


**Figure 4.** The step-by-step construction of the backprojected map for the Tottori fault-station geometry, as described in Fig. 1. The slip function is zero everywhere on the fault, apart from a square anomaly, the boundaries of which are superimposed on the pictures. Each map (starting from the top left panel) is achieved by the addition of the contribution of a single station. Receivers are ordered as follows: SMNH12, SMN004, SMN001, TTR006, OKY004 and HRS021. When a single contribution is backprojected on the fault, the ray theory cannot distinguish which points along the same isochrone provide effective dislocation. The larger the number of stations, the more precise the location of the anomaly will be, although the final image is defocused along the dip direction.

In Fig. 4, we show the step-by-step construction of the slip map, through the addition of the contributions of each station, one at a time. The first panel picture (top left) represents the contribution of the station SMNH12. As expected, the backprojection cannot distinguish which zones have provided effective dislocation along the isochrones.

The larger the number of the contributions that come from the other receivers, the more accurate is the location and the shape of the slip anomaly. However, at the end of the process, the final image remains defocused, and its boundaries describe a smiling anomaly that is distorted along the vertical direction. Lack of resolution along the dip direction is characteristic of vertical strike-slip faults, when using only body waves to retrieve slip images. In this case, all the receivers are located on the same side with respect to the fault and the vertical path of the isochrones does not significantly change for different stations. In Fig. 5 the backprojection is shown for the same source–receiver configuration, but the dip of the fault is now  $20^\circ$ , with the depth of the hypocentre fixed at 13.5 km. In this case, the final image is distorted along an almost horizontal direction.

Finally, since the seismic moment is likely to be conserved on the whole fault, the absolute value of the slip in the anomaly is lower (in this trial it is reduced to  $1/10$  of the true value in the anomaly).

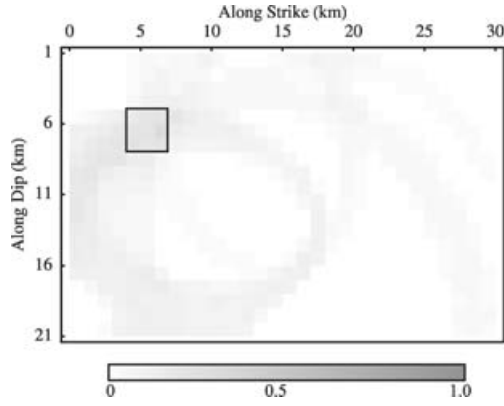


**Figure 5.** Back projection for the same source-station configuration as in the Fig. 4, but for a fault dipping at  $20^\circ$ . The defocusing is now along a quite horizontal direction.

#### 4.2 Image Green functions

In this section, a detailed analysis of the defocusing effect is provided. If the fault has been subdivided into  $h$  elementary subfaults,  $\{Q_1, Q_2, \dots, Q_h\}$ , the associated space in which the slip is allowed to vary is  $\mathbb{R}^{h+}$  (if the slip direction is defined by the rake, the slip value in any subfault is required to be positive). Consider the canonical basis of  $\mathbb{R}^h$ ,  $\{\mathbf{e}_1, \mathbf{e}_2, \dots, \mathbf{e}_h\}$ : a slip map  $\mathbf{U} = (U_1, U_2, \dots, U_h)$  can be decomposed onto it as:

$$\mathbf{U} = \sum_{i=1}^h U_i \mathbf{e}_i$$

Here,  $U_i$  is the slip value in the  $i$ th subfault, and  $U_i \geq 0$  for any  $i$ , because of the positivity constraint. A vector of the canonical basis  $\mathbf{e}_i$  represents the map having a unit slip in the  $Q_i$  cell and zero elsewhere. Synthetic seismograms can be computed and backprojected from each of these elementary maps. The final map  $\mathbf{F}_i$  can be described using the same canonical basis, yielding:

$$\mathbf{F}_i = \sum_{j=1}^h F_{ij} \mathbf{e}_j$$

The matrix  $\mathbf{F}$  is the Green function of the method, which we refer to as *Image Green function*. In Fig. 6 the two *canonical* maps ( $\mathbf{e}_1$  and  $\mathbf{e}_{390}$ ) and the corresponding image Green functions ( $\mathbf{F}_1$  and  $\mathbf{F}_{390}$ ) are represented for the same synthetic example, as used in the previous section. We can see that the largest amount of slip is retrieved in the cell where the anomaly was originally located, although slip values different from zero occur also in those zones that are crossed on average by the same set of isochrones. Hence, the properties of the matrix  $\mathbf{F}$  can be summarized in diagonal dominance, sparsity and a few off-diagonal terms. We will demonstrate that the matrix  $\mathbf{F}$  is also the operator that controls the defocusing effects on the backprojected slip images. In this case, it is sufficient to show the linearity of the forward and inverse problems with respect to the slip function.

If the initial slip map is  $\mathbf{U}$ , from discretization of eqs (2)–(5), the displacement value at the  $k$ th station and  $n$ th time is:

$$D_{kn} = \sum_{i=1}^h K_i^c \frac{R_{ik}^c}{r_{ik}^c} C_{ik} \mathbb{L}_{kn}|_{Q_i} U_i, \quad (13)$$

with the index  $i$  referring to the  $i$ th subfault and  $\mathbb{L}_{kn}|_{Q_i}$  to the length of the isochrone  $\mathcal{L}_{jn}$  inside  $Q_i$ . No summation is assumed on repeated indexes. Eq. (13) can be summarized as follows:

$$D_{kn} = \mathbf{M}_{kn}^{\text{for}} \cdot \mathbf{U}, \quad (14)$$

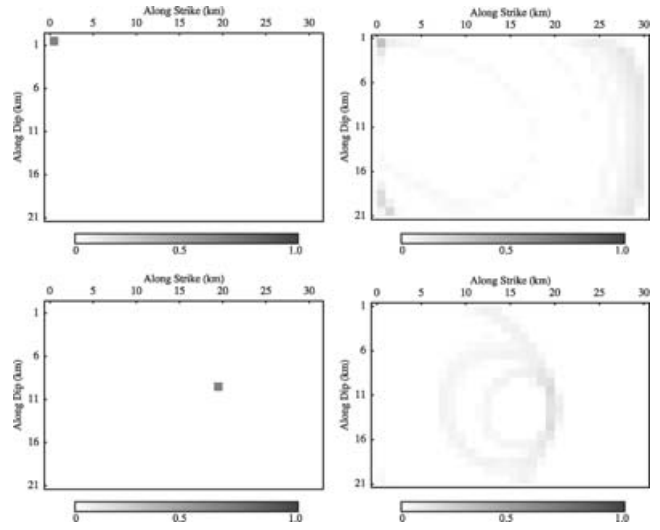


**Figure 6.** Two elementary sources and the corresponding image Green functions. On the right-hand side there are the maps that are obtained by the back-projection of the synthetics evaluated for the maps plotted on the left-hand side.

where  $\mathbf{M}_{kn}^{\text{for}}$  is a vector with complex values. In accounting for the phase shifts, the displacement is:

$$D_{kn} = [\text{Re}(\mathbf{M}_{kn}^{\text{for}}) + \text{Im}(\mathbf{H}\mathbf{M}_{kn}^{\text{for}})] \cdot \mathbf{U}, \quad (15)$$

where  $\mathbf{H}$  is the Hilbert discrete operator. Therefore, the forward modeling can be described by a three-entries matrix  $\mathbf{G}^{\text{for}}$ , such that  $\mathbf{D} = \mathbf{G}^{\text{for}}\mathbf{U}$ .

On the other hand, from eqs (10) and (11), the backprojected displacement  $\mathbf{U}^*$  is obtained from the data matrix  $\mathbf{D}$  as follows:

$$U_i^* = \sum_{j,n} w_j \frac{\mathbb{L}_{jni}}{\sum_m \mathbb{L}_{jmi}} \frac{D_{jn}}{L_{jn}}$$

where  $\mathbb{L}_{jni} = \mathbb{L}_{jn}|_{Q_i}$ . We can summarize the scalar products as follows:

$$U_i^* = \mathbf{G}_i^{\text{back}} : \mathbf{D}. \quad (16)$$

Therefore, the backprojection is also a linear function, the associated operator of which is the three-entries matrix  $\mathbf{G}^{\text{back}}$ .

Since both of the relations (15) and (16) are linear, the matrix  $\mathbf{G} = \mathbf{G}^{\text{back}} : \mathbf{G}^{\text{for}}$  satisfies the relation:

$$\mathbf{U}^* = \mathbf{G}\mathbf{U}. \quad (17)$$

If  $\mathbf{U}$  is any vector  $\mathbf{e}_i$ , the  $i$ th column of  $\mathbf{G}$  is the  $i$ th image Green function. Therefore,  $\mathbf{G} = \mathbf{F}$ .

Assuming zero error on data, the retrieved solution from the back-projection is the true slip on the fault, convolved with the image Green function. Due to its diagonal dominance, the matrix  $\mathbf{G}$  is expected to be invertible and the backprojection effect can be removed by deconvolution. However, non-linear effects owing to the velocity structure and the source-station geometry as well as noise on data need to be accounted for, within the physical constraint  $U_i \geq 0$ . A regularization in the linearized inversion is too expensive in terms of computational costs, to be unfeasible when also inverting for the rupture velocity. Therefore, we proceed to reduce the defocusing effect using an iterative procedure.

#### 4.3 Restarting

In the example analysed at the beginning of this section, the defocusing arises both from an intrinsic resolution, owing to the fault-station

configuration, and from the initial hypothesis, according to which the slip is spread uniformly along the isochrones. This convolutional effect, that has been analysed in the previous section, could be removed by using iterative techniques. In the iterative back projection techniques (Invanson 1983; Olson 1987; Beroza & Spudich 1988), the solution retrieved at the  $n$ th step can be obtained by back propagation of the residual between data and synthetics evaluated on the  $n - 1$ th model. Stability is additionally enforced by damping the contribution of small eigenvalues, when the transpose matrix associated to the linear problem approximates the inverse matrix. Here we investigate another class of more intuitive iterative backprojections. When a first backprojected map is available from the data, it can be used as *a priori* information for a new backprojection. In this case, at the  $n$ th iteration, we re-run the backprojection on the original set of data, by assuming that the slip is no longer spread uniformly

along the isochrones, but the weight in the distribution now depends on the  $n - 1$ th slip solution. We refer this iterative procedure to as ‘restarting’, by similarity with restart algorithms in iterative solvers of linear systems. The improvement in the successive maps needs to be anchored to a comparison with the data. Through this paper, we evaluate the distance between synthetics and data with the  $L^1$  norm, because this limits the importance of the high-amplitude values with respect to the whole signal. Finally, this procedure can be stopped when no additional gain is provided by the successive backprojected map during the iterative process, or, in any case, when an imposed maximum number of iterations is reached.

In the following, the method is applied to the synthetic data set described in the previous section. In Fig. 7, the backprojected maps have been plotted after 1, 2, 3 and 15 iterations. In addition the histograms below each map represent the comparisons between the

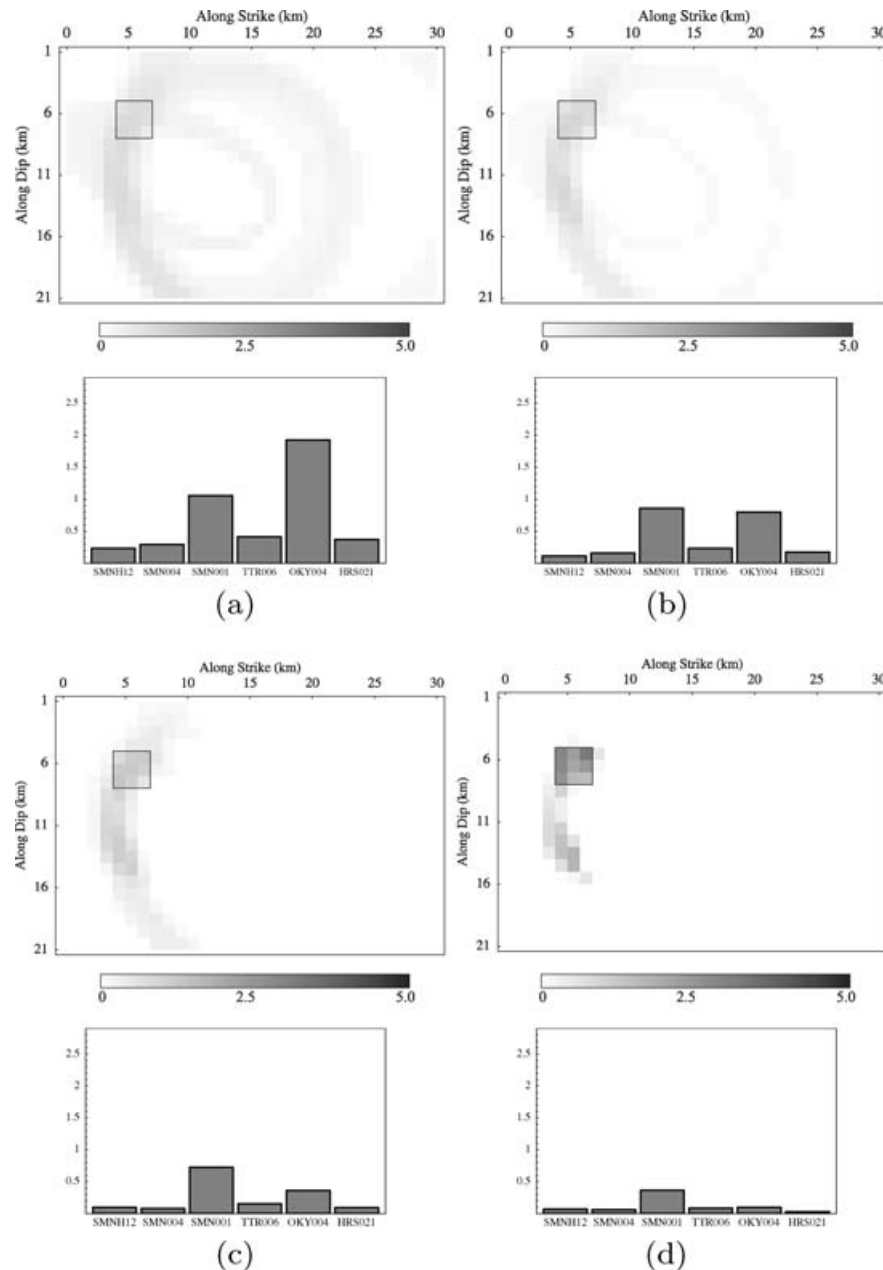


**Figure 7.** Slip maps after 1(a), 2(b), 3(c) and 15(d) iterations in the restarting. Below each map, the histograms represent the misfit between the synthetics and the data, which is singled out station by station.

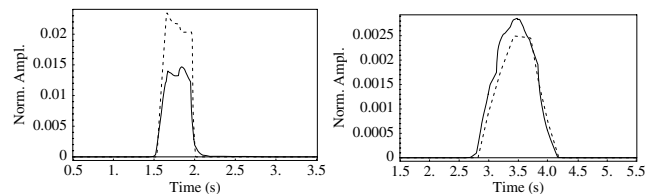


**Figure 8.** Comparison between synthetics evaluated from the original slip map with a focalized anomaly (solid line) and the final backprojected map, obtained by restarting after 15 iterations (dashed line). For the station SMN001-East component (left panel) there is a significant discrepancy due to directivity; for the station SMNH12-North component (right panel) the fit is really good.

synthetics and the data singled out station by station (our data set is itself a collection of synthetic data). As far as the procedure progresses, the absolute value and the original shape of the anomaly are more and more retrieved, within a focalization of the final image around the original patch. In the final map, the slip reaches the 80 per cent of its true value and the original shape is well reproduced, although it is slightly distorted downwards. From the histograms, a significant gain can be observed for the low-order terms (between 40 and 50 per cent for both the first and second corrections), while the gain after 15 iterations is only of 10 per cent when compared to the third map. In this case, the restarting can go on for many iterations (about 30), since the data have been generated with the same approximations as the synthetics.

In conclusion, focused (after 15 iterations) and defocused (after only 3 iterations) maps could be confused by the inversion, when comparing synthetics to data at the chosen set of stations. Moreover, when dealing with real data, the defocused map is preferred. In fact, the restarting procedure is expected to be stopped after a few iterations because other approximations, such as noise on data, inaccuracies in the Green function, the fault geometry and the focal mechanism, introduce significant errors, when compared with high-order terms in the restarting.

Finally in Fig. 8 we compare synthetics and data for stations SMN001 and SMNH12. The fit is particularly good for the lateral station SMNH12, as well as for the other stations (see histograms in Fig. 7), with the exception of the station SMN001. In fact, the latter is the only directive station, given the location of the anomaly on the fault plane. For the chosen location of the anomaly, it is the only directive station. As it can be argued from the inspection of Fig. 4 step 3, the isochrones corresponding to SMN001 have a more eccentric shape than in the case of lateral and antidirective stations. Hence, when the slip anomaly is localized, directive stations show to be more sensitive to the vertical blurring of the final slip image.

## 5 RUPTURE VELOCITY ESTIMATION

Up to this stage, we have set up an algorithm, that allows for a slip map to be obtained, if the rupture velocity distribution is assumed on the fault surface. Usually the rupture velocity is not known and it is expected to be a rough function, even in its kinematic description (Beroza & Spudich 1988; Cotton & Campillo 1995). However, the backprojection technique allows for a slip map to be associated to any assumed rupture velocity function. When a collection of coupled slip map-rupture velocity map is built up, the best will represent the solution of the considered inverse problem, according to a fitness criterion. The latter function can be defined directly on the slip map, within an assumption of some roughness principle (for instance, we

could prefer maps having focalized high-slip zones). In this case, the solution runs the risk of not being correlated with the data. If the restarting procedure is adopted to reduce the defocusing, the mis-fit function is naturally defined in the data space and the same criterion of comparison (the  $L^1$  norm) can be adopted for the inversion. In this case, the parameter space contains all of the possible values  $\{V_1, \dots, V_N\}$ , that the rupture velocity can assume at a set of control nodes  $\{\mathbf{x}_1, \dots, \mathbf{x}_N\}$  on the fault. The minimum is searched for using the genetic algorithm, which represents a good compromise between the computational costs and the global exploration (Goldberg 1989; Charbonneau 1995).

The solution of the kinematic problem has been translated into a problem of minimum searching, in which the rupture velocity is the only parameter involved, while the slip function is automatically provided by the backprojection of recorded ground-motion amplitudes. This formulation simplifies the standard non-linear inversions that search for joint estimates of slip and rupture velocity. Here the intrinsic separation of the parameters relies on the hypothesis that the backprojected map is the optimal and unique solution for a given rupture velocity map. In this case, when looking at the whole parameter space, the one defined on both the rupture velocity and the slip, we are confining the exploration along the valley of the minima with respect to the slip. Non-linear effects on the slip, that may arise from the fault geometry, the positivity constraint and the restarting process, could result in jumps from one valley to another one. However, smoothness on the slip, automatically provided by the defocusing, warrants stability because of a continuous dependence on the data. (for two given close rupture velocity maps  $\mathbf{V}$  and  $\mathbf{V} + \Delta\mathbf{V}$ , the difference in the corresponding slip maps still remains small).

In addition, the two-step inversion is built up on two separated parametrization grids, which do not need to overlap. Since only the rupture velocity is involved in the kernel of the non-linear inversion, we set the dimension of the rupture velocity space  $N$  smaller than the number of subfaults  $h$  in which the slip is defined. This choice relies on the hypothesis that the correlation between the rupture velocity and the slip is resolved at wavelengths larger than the resolution of the slip, when looking at the amplitudes of the displacement records. This is for two reasons. First the rupture velocity is chosen as a parameter because it easily guarantees the causality in the propagation of the rupture front, but it is not directly involved in the inversion. In the place of it, inversions algorithms require the rupture times, which are a smoother function, obtained from the velocity by integration. Second, when using displacement records, the steep changes in the speed of the rupture front are smoothed.

Finally, the velocity is interpolated onto the finer grid of the subfaults, using a the first-order Lagrange expansion.

### 5.1 Numerical inversion

In this section, a synthetic example is provided to analyse the inversion of the rupture velocity. The synthetics have been computed for the source-receiver geometry defined in Fig. 1, with the same set of stations, as used in the previous section. The original slip map is uniform ( $\delta u = 1$  m), with two anomalies. A positive anomaly is located in the northern part of the fault, and the slip inside is five times larger than elsewhere. A zero patch is instead close to the hypocentre. The boundaries of the anomalies have been superimposed on the final slip map of Fig. 9(a). The rupture velocity is also uniform ( $v = 2.3$  km s<sup>-1</sup>), with an anomaly in the northern part, where the value of the velocity is  $v = 2.8$  km s<sup>-1</sup>. The shape of the anomaly is sketched on the map of Fig. 9(b).

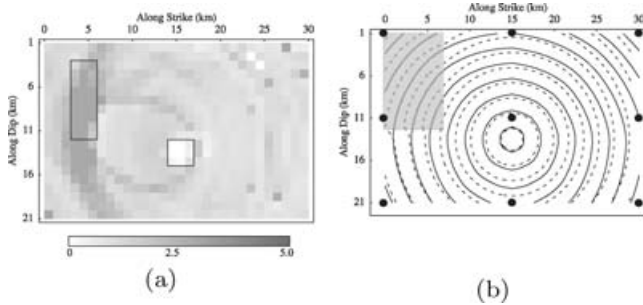


**Figure 9.** In the left panel, the backprojected slip map from the inversion is compared with the original model (the two boxes represent the location of the anomalies). On the right, the retrieved rupture times (dashed line) are compared with the original ones (the box here marks the location of the rupture velocity anomaly). In spite of the different rupture times, the original anomalies in the slip map are mostly retrieved, although the shape of the high slip patch is lengthened in the dip direction.

The fault has been subdivided in  $30 \times 20$  squared subfaults, in which the slip is assumed to be uniform. We have used nine nodes on the fault plane to anchor the velocity value (the points in Fig. 9b). In this test, the *true* model does not belong to the solution space. For the inversion, we used a genetic algorithm with a population of 30 genotypes and we let it to evolve for 300 iterations, constraining the velocity values to range between 2 and  $3 \text{ km s}^{-1}$ . The retrieved model is plotted in Fig. 9.

When comparing the retrieved slip model with the original one, the location of the high slip anomaly is again retrieved, with a lack of resolution along the vertical direction. The value of the slip in the anomaly is approximately the initial one ( $\delta u$  ranges between 4 and 4.8 m). The values of the velocity obtained on the northern side are (from the top):  $v_1 = 2.7 \text{ km s}^{-1}$ ,  $v_2 = 2.6 \text{ km s}^{-1}$ ,  $v_3 = 2.35 \text{ km s}^{-1}$ . Elsewhere the mean value is about  $2.25 \text{ km s}^{-1}$ . Although the velocities are on average very similar, the rupture times are quite different (Fig. 9b). Finally, comparison between the data and the synthetics is shown in Fig. 10. For the considered model, the fit is really good and the differences exist only in some high-frequency details (most of all for the directive station SMN001).

## 6 THE APPLICATION TO REAL DATA

The 2000 Tottori earthquake has been recorded by the K-net and Kik-net stations, that are provided with accelerometers with a low-

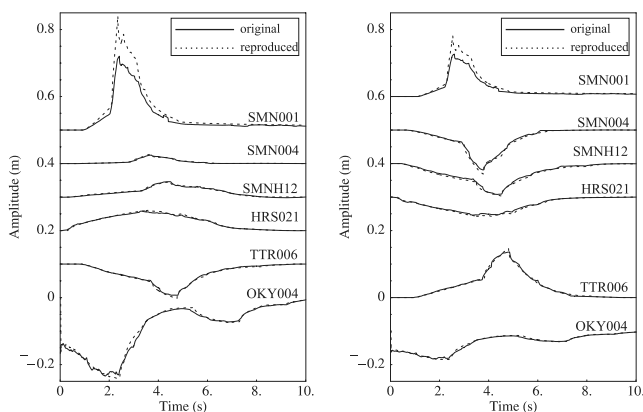


**Figure 10.** Comparison between the original data and the synthetics evaluated from the final rupture velocity map and the consequent slip of Fig. 9.

pass response, a cut-off frequency of 30 Hz and absolute time. In the selection of the stations, we discarded the closest ones (which have a distance from the fault less than 10 km), to guarantee the far-field condition. The final set of records consists of 12 stations, that are located in the epicentral distance range of 20–50 km (Fig. 1).

As required by the backprojection, the displacement records are directly obtained by double integration from accelerations, and the low-frequency trend has been removed through a baseline correction, using a fourth-order polynomial interpolation on the noise before and after the signal (Boore 2001; Zhu 2003, Boore & Bommer 2005). This procedure allows for the retrieval of the displacements with proper sign. Moreover, in the comparison between synthetics and data, we add a band-pass filter. The lower frequency has been chosen to be 0.1 Hz, in order to have at least two to three wavelengths between any subfault and any station (far-field condition). The maximum frequency has been set at 0.5 Hz as the limit, at which the *S* signal remains coherent. Beyond that frequency, the pollution of additional reflected and diffracted phases from the 3-D propagation becomes significant. To infer the upper threshold, we look at the stability of the motion on the *S* train in the data by polarigrams. The selection of the *S* wave in the seismograms has been done by limiting the record window by the theoretical first arrival *S* time, which can be obtained from the 1-D propagation model of Table 1. This time has been checked against the direct picking of the *S* wave, when it was possible. In Fig. 11 we have compared polarigrams for

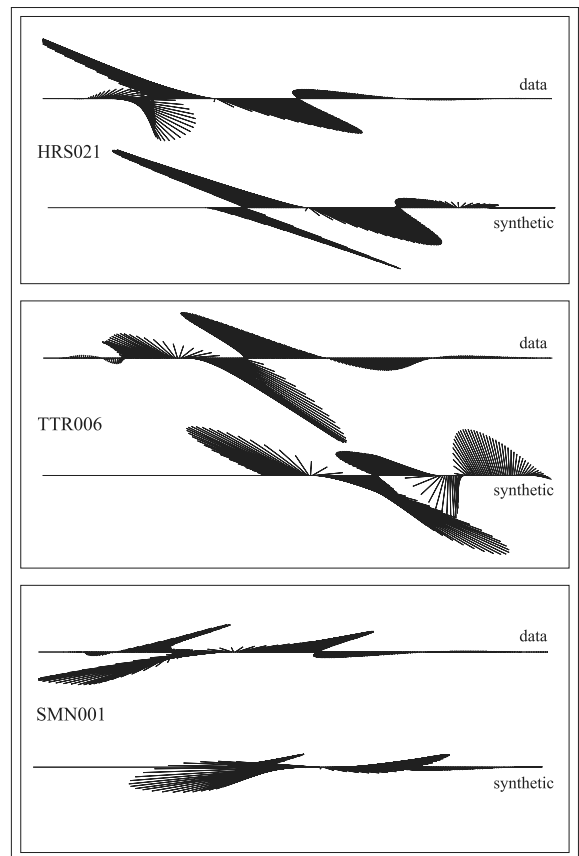


**Figure 11.** Comparison between the polarigrams from the data and the synthetics for a southward station (HRS021), a lateral one (TTR006) and a northward one (SMN001). The direct *S*-train is expected to have an almost constant direction with time. For the lateral station TTR006 a change of direction in the final part of the synthetic, which is not present in the record, could indicate that the slip is at low level near the ends of the fault.

the data and the synthetics, the latter obtained with a constant slip and a constant rupture velocity of  $v = 2.4 \text{ km s}^{-1}$ . We show some examples for the stations HRS021, TTR006 and SMN001, which are located southwards, laterally and northwards with respect to the fault plane.

For all of the synthetics, the orientation does not change as the rupture moves away from the hypocentre, at least in the first part of the record. Hence, we can argue that the  $S$ -wave train is expected on average to follow an almost constant direction with time for any station. The lateral station TTR006 shows good agreement with the expected direction. The final change in the synthetics reflects the changes of sign in the radiation pattern for the isochrones located close to the ends of the fault. This feature, which is present for all the lateral stations (TTRH04, SMNH12, SMN003, SMNH02), is not seen in the data, indicating that the slip should be at a low level there. At the station HRS021, the direction of the motion on the horizontal component fits the theoretical one everywhere, except at the beginning of the signal, where the amplitudes may correspond to a foregoing phase.

After selecting the  $S$  window for all of the stations, the inversion has been performed by backprojecting the displacement amplitudes. For this purpose, the fault has been discretized into squares of size 1 km, providing  $30 \times 20$  subfaults. The rupture velocity has been discretized by using nine control points that are equally spaced along the strike and the dip directions. The cost function is

$$f(\mathbf{V}, \mathbf{d}) = \sum_i w_i \sum_j |d_{ij} - d_{ij}^{\text{syn}}(\mathbf{V}, \mathbf{U}^{\text{back}}(\mathbf{V}))|, \quad (18)$$

where  $d_{ij}$  is the observation at the station  $i$  and at time  $j$ , and  $d_{ij}^{\text{syn}}$  is the value of the synthetic at the same time and station. The latter depends on the velocity values  $\mathbf{V}$  at the control nodes and on the backprojected map  $\mathbf{U}^{\text{back}}$ . For this example, the weights  $w_i$  are associated to the maximum amplitude measured on each component of the displacement records (We remark that, for any station, the two horizontal components are considered as independent traces to be backprojected).

In the Figs 12–14 the results of the inversion have been analysed. The slip map (Fig. 12) has been compared directly with the solution provided by Iwata & Sekiguchi (2002). We retrieve two different patches of slip. The major one starts above the hypocentre, close to the surface and goes down southwards until to reach the bottom of the fault. The second one is located northwards at a depth between 10 and 18 km. The reliability of the images can be analysed with the help of the image Green functions, associated to the final solution. As far as we look at the defocusing of the discrete pixels in the major patch, the backprojected images are mainly correlated along the dip direction, downwards. Hence we can argue that the slip close to the surface is real. At depths larger than the hypocentre location, the lack of resolution does not allow to infer how deep is the anomaly. Moreover the focusing of energy at the bottom is probably an artefact, because the isochrones of both patches intersect in that region. If we raise up the bottom of the fault, such a focusing effect is largely reduced. On the other hand, the width of the other anomaly is larger and its location is harder to be defined. Such blurring effects seem to be also present in the Iwata & Sekiguchi (2002) slip map. Although we obtain high slip concentration close to the surface, as in most of the kinematic inversions of Tottori earthquake, we found non-symmetric slip distribution above the hypocentre, as retrieved by Yagi (2001) and Semmane *et al.* (2005). The same result was achieved by Iwata & Sekiguchi (2002). A southern predominance of the slip can be confirmed by the aftershock location

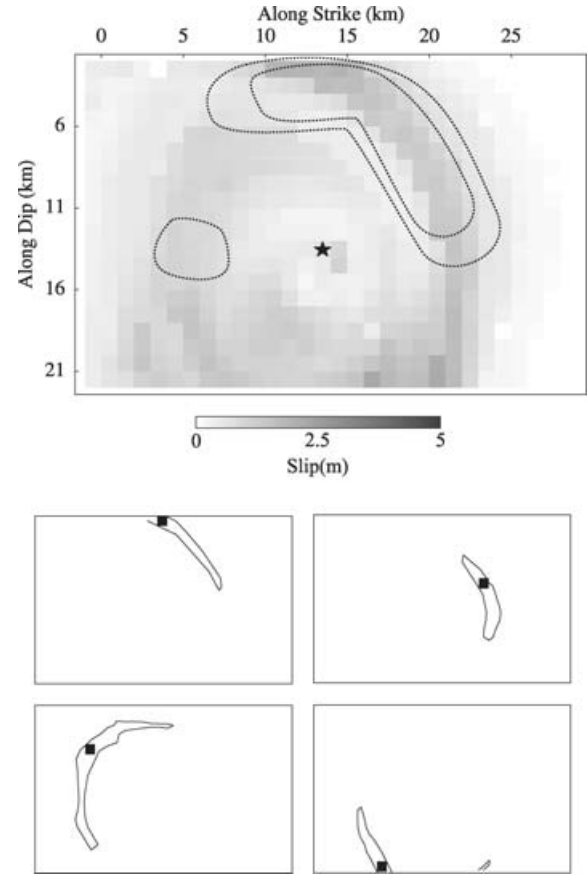


**Figure 12.** In the upper part, the slip map, as retrieved by the backprojection, is compared to the map provided by Iwata & Sekiguchi (2002). We found two major asperities: the first located in the shallower part of the fault, southwards; the second one northward, with less defined boundaries. In the lower part of the pictures we show the defocusing effect of some pixels through the image Green functions. We see that, when the pixel is located in the major patch, the blurring effect is mainly directed downwards. We can argue, hence, that the large values of the slip close to the surface are real.

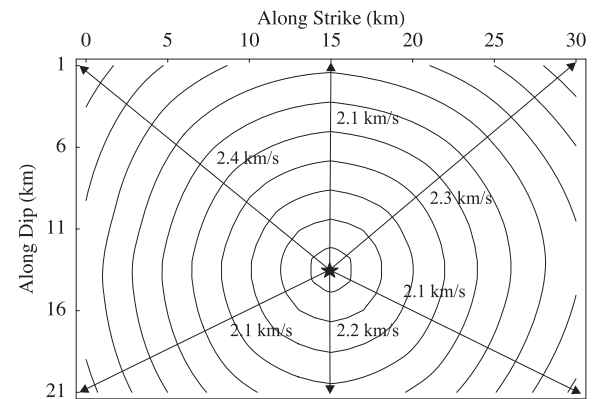


**Figure 13.** Rupture fronts and mean values of the rupture velocity as retrieved by the inversion.

(Fukuyama *et al.* 2003), which indicated that a large number of the earliest aftershocks occurred in the SE part of the fault and then they migrated northwards some time after the main shock. The seismic moment, as retrieved by the inversion, is  $2.67 \cdot 10^{19} \text{ N m}$ , which corresponds to a seismic magnitude of  $M_w = 6.88$ . Compared to the strong-motion solution of Semmane *et al.* (2005) ( $M_w = 6.8$ ), the

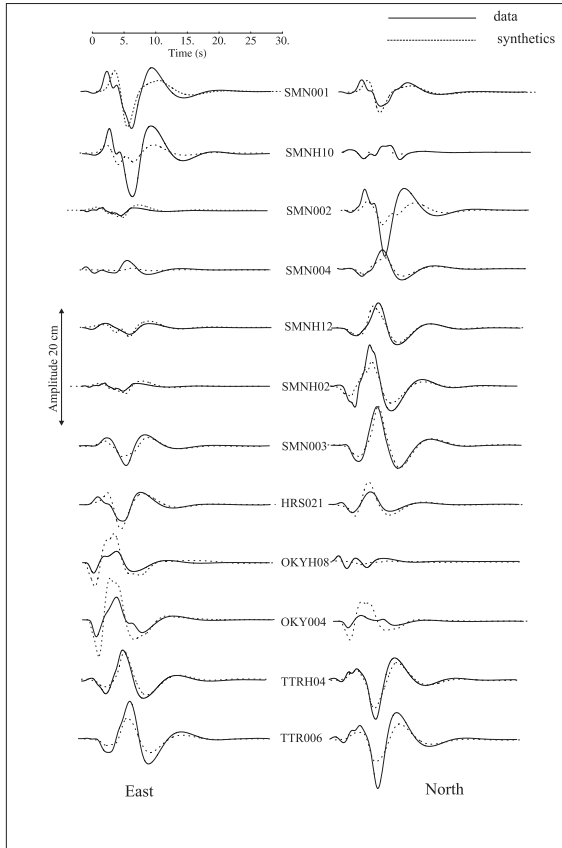


**Figure 14.** Comparison between the data (solid lines) and the synthetics (dashed lines), for the horizontal East and North components, respectively. A reasonable agreement is seen for the lateral stations, while more inconsistencies occur for the stations OKY004, OKYH08, SMNH10 and SMN002.

slightly high-value of the seismic moment can be justified by noting that for this magnitude, the selected frequency band (0.1–1.0 Hz) does not capture the flat part of the spectrum, being the minimum frequency 0.1 Hz beyond the corner frequency for the *S* waves. The mean value of the rupture velocity is  $2.2 \text{ km s}^{-1}$ , with almost regular fronts (Fig. 13). Finally, the comparison between the data and the synthetics shows good agreement at the lateral stations (SMN003, SMN004, SMNH02, SMNH12, TTRH04 and TTR006). Larger amplitudes in the synthetics for the directive stations OKY004 and OKYH08 could be indicative of an artefact, that is, the extension of the slip downwards at the bottom of the fault (as observed also in the synthetic example of Section 4.3). Some inconsistencies are also present for the northern stations SMNH10 and SMN002, but not for SMN001, for which the displacement amplitudes are reasonably retrieved. As argued by Semmane *et al.* (2005), low-frequency amplification could occur at those stations, due to site effects associated with the marine sedimentary coverage.

## 7 DISCUSSION AND CONCLUSIONS

Recently, the demand of fast and reliable algorithms for the inversion of the source parameters is increasing specially considering near-real time or fast assessment of ground motion shaking and damages soon after the occurrence of moderate to large earthquakes. In this paper, we have proposed a fast technique for the retrieval of slip images from the backprojection of near-source, high frequency displacement amplitudes, as recorded by dense strong-motion arrays

around potentially causative faults. Starting from a null information on the slip distribution, the slip has been distributed uniformly along the corresponding isochrone. The combination of information coming from different stations allows to enhance the high-slip zones, although a part of the energy is not focalized and remains in any case spread out elsewhere on the fault plane, following the average direction of the isochrones. This is mainly due to the source-stations geometry. Information about the resolution of the images is achieved by looking at the image Green functions, which measure the distortion of any original pixel as an effect of the geometry of the fault and the receivers. For the particular case of strike-slip faults, we observe a lack of resolution along the vertical direction, which does not allow to precisely retrieve the depth of the anomalies.

We also demonstrate that the defocusing effect can be described by a linear operator and, therefore, it could be removed from the final map. Because of non-linear effects, that arise from the geometry, the positivity and the smoothness of the slip function, the inversion requires some additional constraints. As a consequence, the matrix inversion becomes unfeasible in a inversion kernel, when one is also interested into searching for the rupture velocity model. Instead of a full deconvolution, a partial removal of defocusing can be achieved if we re-run the backprojection assuming, as initial model, the slip distribution obtained at the previous iteration ('restarting'). This iterative method, however, requires a comparison between the synthetics and the data to define a stopping criterion. According to our numerical trials, a few steps are sufficient to significantly improve the data fit, whereas high-order terms provide weaker corrections (fractions of percent). In this case, the restarting procedure increases the computation by two to five times, which is still a low cost, as compared to the matrix inversion in an LSQR approximation.

We remark that the stability of the back propagation is warranted when the contribution of a whole isochrone at a given station is significantly larger than the noise level. For this reason we prevent the backprojection of that isochrones, along which the radiation pattern changes its sign. Therefore, this method will work better for earthquakes of magnitude between 4.5 and 6.0, and stations located between 30 and 200 km. In this case, we deal with fault lengths of 2 to 10 km and receivers at several radii from the fault.

The rupture velocity controls the isochrones shapes on the fault plane and it should be assumed *a priori* to compute a backprojected slip map. As the rupture velocity is unknown, we proposed the building up of a collection of rupture velocity maps, with a slip map associated to each of them by backprojection. In this case, the solution of the kinematic source problem can be chosen within the rupture velocity map' collection according to the same criterion that is based on the misfit of the data. When applying this procedure, we intrinsically separate the kinematic inversion into two parts: the rupture velocity is retrieved from a fully non-linear inversion, while the slip map is consequently provided from the backprojection. This procedure allows to limit the dimension of the parameter space in the non-linear inversions. Moreover, the same discretization for both the rupture velocity and the slip is not necessary: on the contrary, since the slip grid is related to the Fraunhofer approximation, it is expected to be finer than the rupture velocity grid, which is related to the computational costs and the efficiency of the global searching algorithm. Finally, the stability of the inversion is reinforced by the implicit smoothness of the slip maps. This assures that close rupture velocity maps do provide similar slip maps.

The choice of a double parametrization relies on the hypothesis that the correlation between rupture velocity and slip can be resolved at wavelengths larger than the spatial resolution of the slip, when comparing the amplitudes of the displacement records. The

synthetic example as well as the Tottori inversion, compared to the solution of Iwata & Sekiguchi (2002), show that high slip zones can be retrieved (in location and amplitude) even if the rupture times are quite different. That opens a question about the way in which the rupture velocity is used to retrieve the displacement amplitudes. It is possible that different parametrizations of the rupture velocity lead to the same homogenized model, as it is seen from the low-frequency displacements records. A more coherent description of the rupture velocity could come from the dynamic modelling as well as from the near-fault high frequency observations.

When applying the backprojection to achieve the slip map of the 2000 Tottori earthquake, we obtain a very consistent model with that proposed by Iwata & Sekiguchi (2002), the slip being predominantly concentrated near the surface and going down southwards. A second anomaly is located between 10 and 18 km in the northern part of the fault. The value of the seismic moment is also consistent with other studies on the same earthquake.

In conclusion since the problem is linear with respect to the slip, the backprojection can be substituted by a linear inversion of eqs (2)–(5) or even of eq. (1), when the complete wavefield is taken into account. In this case, more accurate solutions will be provided for the slip, but at substantially higher computational costs.

## ACKNOWLEDGMENTS

We are grateful to two anonymous reviewers, who helped to improve the paper. This work has been supported by the EU-Project spice.

## REFERENCES

- Aki, K., 1968. Seismic displacements near a fault, *J. geophys. Res.*, **73**, 5359–5376.
- Aki, K. & Richards, P.G., 1980. *Quantitative Seismology*, Eds. Freeman & Co., New York.
- Anderson, J.G., 1991. Strong motion seismology, *Rev. Geophys.*, 700–720.
- Bernard, P. & Madariaga, R., 1984. A new asymptotic method for the modeling of the near-field accelerograms, *Bull. seism. Soc. Am.*, **74**, 539–557.
- Beroza, G.C. & Spudich, P., 1988. Linearized inversion for fault rupture behavior: application to the Morgan Hill, California, earthquake, *J. geophys. Res.*, **93**, 6275–6296.
- Bindi, D. & Caponetto, A., 2001. Tomographic imaging of the earthquake source: numerical validation in two-dimensional approximation, *J. geophys. Res.*, **106**(B4), 6643–6656.
- Boore, D.M., 2001. Effects of the baseline corrections on the displacements and response spectra for several recording of the 1999 Chi-Chi, Taiwan earthquake, *Bull. seism. Soc. Am.*, **91**, 1199–1211.
- Boore, D.M. & Bommer, J.J., 2005. Processing of strong motion accelerograms: needs, options and consequences, *Soil Dyn. Earth. Eng.*, **25**, 93–115.
- Bouchon, M., 1979. Discrete wave number representation of elastic wave fields in three-space dimensions, *J. geophys. Res.*, **84**(B7), 3609–3614.
- Chapman, C.H., 1985. Ray theory and its extensions: WKBJ and Maslov seismograms, *Geophys. J. Int.*, **58**, 27–43.
- Charbonneau, P., 1995. Genetic algorithms in Astronomy and Astrophysics, *Astrophys. J. (Supp.)*, **101**, 309–334.
- Cohee, B.P. & Beroza, G.C., 1994. Slip distribution of the Landers earthquake and its implications for earthquake source mechanics, *Bull. seism. Soc. Am.*, **84**(3), 692–712.
- Cotton, F. & Campillo, M., 1995. Frequency domain inversion of strong motions: application to the 1992 Landers earthquake, *J. geophys. Res.*, **100**(B3), 3961–3975.
- Emolo, A. & Zollo, A., 2005. Kinematic source parameters for the 1989 Loma Prieta earthquake from the nonlinear inversion of accelerograms, *Bull. seism. Soc. Am.*, **95**(3), 981–994 doi:10.1785/0120030193.
- Farra, V., Bernard, P. & Zollo, A., 1986. Fast near source evaluation of strong motion for complex source models, *Geophys. Monograph*, **6**, 121–130.
- Fukuyama, E., Ellsworth, W.L., Waldhauser, F. & Kubo, A., 2003. Detailed fault structure of the 2000 Western Tottori, Japan, earthquake sequence, *Bull. seism. Soc. Am.*, **93**(4), 1468–1478.
- Goldberg, D.E., 1989. *Genetic Algorithms in Search, Optimization and Machine Learning*, Addison & Whesley Pub Co.
- Graves, R.W. & Wald, D.J., 2001. Resolution analysis of finite fault source inversion using 1-D and 3D Green's functions. I. Strong Motion, *J. geophys. Res.*, **106**, 8745–8766.
- Hartzell, S.H., 1978. Earthquake aftershocks as Green's functions, *Geophys. Res. Lett.*, **5**, 1–4.
- Hartzell, S. & Liu, P., 1995. Determination of earthquake source parameters using a hybrid global search algorithm, *Bull. seism. Soc. Am.*, **85**(2), 516–524.
- Heaton, T.H., 1990. Evidence for an implications of self-healing pulses of slip in earthquake rupture, *Phys. Earth planet. Int.*, **64**, 1–20; *Geophys. Res. Lett.*, **27**, 3401–3404.
- Invanson, S., 1983. Remark on an earlier proposed tomographic algorithm, *Geophys. J. R. astr. Soc.*, **75**, 855–860.
- Iwata, T. & Sekiguchi, H., 2002. Source process and near-source ground motion during the 2000 Tottori-ken seibu earthquake (in Japanese with English abstract), *Proc. 11th Japan Earthq. Eng. Symp.*, 125–128.
- Ji, C., Wald, D.J. & Helmberger, D.V., 2001. Source description of the 1999 Hector Mine, California, earthquake, Part I: Wavelet domain inversion theory and resolution analysis, *Bull. seism. Soc. Am.*, **92**(4), 1192–1207.
- Kennett, B.L.N., 2002. *The seismic wavefield. Volume II: Interpretation of seismograms on regional and global scales*, Cambridge University Press, Cambridge.
- Kennett, B.L.N., Marson-Pidgeon, K. & Sambridge, M.S., 2000. Seismic source characterization using a neighborhood algorithm, *Geophys. Res. Lett.*, **27**, 3401–3404.
- Koyama, J., 1997. *The complex faulting process of earthquakes*, Kluwer Academic, Dordrecht.
- Olson, A.H., 1987. A Chebyshev condition for accelerating convergence of iterative tomographic methods—Solving large least squares problems, *Phys. Earth planet. Inter.*, **47**, 333–345.
- Peyrat, S. & Olsen, K.B., 2004. Nonlinear dynamic rupture inversion of the 2000 Western Tottori, Japan, earthquake, *Geophys. Res. Lett.*, **31**, L05604, doi:10.1029/2003GL019058.
- Podvin, P. & Lecomte, I., 1991. Finite difference computation of travel times in very contrasted velocity models: a massively parallel approach and its associated tools, *Geophys. J. Int.*, **105**, 271–284.
- Semmane, F., Cotton, F. & Campillo, M., 2005. The 2000 Tottori earthquake: a shallow earthquake with no surface rupture and slip properties controlled by depth, *J. geophys. Res.*, **110**, B03306, doi:10.1029/2004JB003194.
- Spudich, P. & Frazier, N.L., 1984. Use of ray theory to calculate high-frequency radiation from earthquake sources having spatially variable rupture velocity and stress drop, *Bull. seism. Soc. Am.*, **74**, 2061–2082.
- Vallée, M., Bouchon, M. & Schwarz, S.Y., 2003. The 13 January 2001 El Salvador earthquake: a multidata analysis, *J. geophys. Res.*, **108**(B4), doi:10.1029/2002JB001922.
- Wald, D.J. & Heaton, T.H., 1994. Spatial and temporal distribution of slip for the 1992 Landers, California, earthquake, *Bull. seism. Soc. Am.*, **84**(3), 668–691.
- Yagi, Y., 2001. Source rupture process of the Tottori-ken Seibu earthquake of the October 6, 2000 obtained by joint inversion of the near field and teleseismic data pres. Meeting of Japan Earth and Planetary Science, Tokyo, Japan.
- Zeng, Y. & Anderson, J.G., 1996. A composite source modeling of the 1994 Northridge earthquake, using genetic algorithms, *Bull. seism. Soc. Am.*, **85**, 300–307.
- Zeng, Y. & Chen, C.H., 2001. Fault rupture process of the 20 September 1999 Chi-Chi, Taiwan, earthquake, *Bull. seism. Soc. Am.*, **91**(5), 1088–1098.
- Zhu, L., 2003. Recovering permanent displacements from seismic records of the June 9, 1994 Bolivia deep earthquake, *Geophys. Res. Lett.*, **30**(14), doi:10.1029/2003GL017302.
- Zollo, A. & Bernard, P., 1989. S-wave polarization inversion of the October 1979, 23:19 Imperial Valley aftershock: evidence for anisotropy and a simple source mechanism, *Geophys. Res. Lett.*, **16**, 1047–1050.